ARTICLE IN PRESS

Available online at www.sciencedirect.com

ScienceDirect

Advances in Space Research xxx (xxxx) xxx

ADVANCES IN SPACE RESEARCH (a COSPAR publication)

www.elsevier.com/locate/asr

Environmental impact of object breakup in medium-Earth orbit

Lorenzo Giudici [a,*], Juan Luis Gonzalo [a], Andrea Muciaccia [a], Camilla Colombo [a], Mirko Trisolini [b], Francesca Letizia [c]

[a] Politecnico di Milano, Department of Aerospace Science and Technology, via La Masa 34, Milano 20156, Italy
[b] Vyoma, Karl-Theodor-Straße 55, München 80803, Germany
[c] European Space Agency, Independent Safety Office, Keplerlaan 1, Noordwijk 2201, the Netherlands

Received 26 January 2024; received in revised form 10 May 2024; accepted 5 June 2024

Abstract

Large derelict objects are severely affecting the sustainability of the space environment. This has brought attention on the importance of ranking in-orbit objects and future missions, based on the risk they pose to the proliferation of orbital fragments. To this purpose, several sustainability metrics have been formulated to guarantee a scientific support in the definition of remediation measures, as well as for the identification of safe orbital slots for future missions. The index ECOB (Environmental Consequences of Orbital Breakups) was developed with the objective of measuring the space environmental impact of an object in low-Earth orbit based on the risk it represents for satellites operations. The severity of a breakup was computed as the cumulative collision probability induced by the evolving debris cloud on the active satellites population. In this paper, the ECOB metric is extended to the medium-Earth orbital region, leveraging a density-based multi-dimensional fragments cloud propagator and collision risk estimator, capable of working with any arbitrarily complex orbital dynamics and conjunction geometry. The dependency of the effect of a breakup on the fragmentation orbit's shape and orientation is investigated and discussed. The currently in-orbit missions are eventually ranked based on the proposed metric.
© 2024 COSPAR. Published by Elsevier B.V. This is an open access article under the CC BY-NC-ND license (http://creativecommons.org/licenses/by-nc-nd/4.0/).

Keywords: Space debris; Breakup severity; Sustainability metric in medium-Earth orbit; In-orbit collision risk

1. Introduction

Several studies highlighted how large derelict objects are going to shape the future trend of the space debris environment (Rossi et al., 2015). Nowadays, with greater awareness towards the debris problem, it has become evident how crucial is the evaluation of the impact of a mission or individual object on the long-term sustainability of space. For this reason, several metrics have been developed to rank the risk posed by orbiting objects, as well as by potential future missions, on spacecraft operations. The possible application of these indices is twofold: on the one hand, if applied to the in-orbit objects population, they could point towards the best candidates for Active Debris Removal (ADR). On the other hand, they could support taking go/no-go decisions for future missions, and helping in the identification of orbital slots that can prevent the proliferation of space debris, in case of mission failure.

The majority of the developed sustainability metrics have been formulated as *probability*×*severity*, i.e., as the product between the likelihood of the mission breakup and the effect the fragmentation would have onto the space environment. The *probability* component is historically expressed as function of the debris flux perceived by the ranked object (Rossi et al., 2015; Anselmo and Pardini, 2016; Pardini and Anselmo, 2016; Letizia et al., 2019), miss

* Corresponding author.
E-mail addresses: lorenzo1.giudici@polimi.it (L. Giudici), juanluis.gonzalo@polimi.it (J.L. Gonzalo), andrea.muciaccia@polimi.it (A. Muciaccia), camilla.colombo@polimi.it (C. Colombo), mirko.trisolini@vyoma.space (M. Trisolini), francesca.letizia@esa.int (F. Letizia).

https://doi.org/10.1016/j.asr.2024.06.012
0273-1177/© 2024 COSPAR. Published by Elsevier B.V.
This is an open access article under the CC BY-NC-ND license (http://creativecommons.org/licenses/by-nc-nd/4.0/).

Please cite this article as: L. Giudici, J. L. Gonzalo, A. Muciaccia et al., Environmental impact of object breakup in medium-Earth orbit, Advances in Space Research, https://doi.org/10.1016/j.asr.2024.06.012

distance of monitored conjunctions (McKnight et al., 2021), or combination of the two (McKnight et al., 2017). Two main methodologies have been pursued for the evaluation of the *severity* component. The first approach does not involve any simulation and aims to obtain an immediate assessment of the consequences of the potential breakup based on relevant factors, such as the properties and location of the fragmentation, or derivatives of these. For example, in the CSI (Criticality of Spacecraft Index) proposed by Rossi et al. (2015) the *severity* is computed as the lifetime of a naturally decaying spacecraft at the altitude of the object to be ranked, scaled by a factor that accounts for its mass. The index was subsequently extended to the ranking of large constellations (Rossi et al., 2017) and to the definition of a criticality distribution as a function of altitude over the entire Low-Earth Orbit (LEO) region (Bombardelli et al., 2017). In Anselmo and Pardini (2015), Pardini and Anselmo (2018), the consequence of the fragmentation is proportional to the Collisional Debris Cloud Decay of 50% (CDCD50), i.e., the time needed for the decay of 50% of the fragments cloud generated by the catastrophic collision of the analysed object. CDCD50 functions are created a priori to speed up the computation process (Anselmo and Pardini, 2017). A second approach involves the characterisation and propagation of the potential breakup. With the work by Letizia et al. (2016b, 2017) on the index ECOB (Environmental Consequences of Orbital Breakups), the effect of the fragmentation is formulated as the impact it would cause on the spacecraft operations in the same region, monitoring the cumulative collision probability with a set of targets representative of the active satellites population. The strength of this index is that it provides a direct measure of the potential loss for the spacecraft operators. The ECOB metric has been extensively adopted by the European Space Agency (ESA), e.g., for the evaluation of the environmental impact of the ESA fleet (Letizia and Lemmens, 2021) and for the assessment of the beneficial effect of mitigation strategies. In the work by Ruch and Revelin (2020) and Omaly et al. (2023), the CSI is adopted for the identification of a preliminary list of most-concerning objects, which is subsequently refined through the ECOB index and additional contributions, based on how the object is built and operated (e.g., post-mission disposal rate).

Alternatively, sustainability metrics have been defined based on long-term simulations of the space debris environment (Bastida Virgili and Krag, 2013; Lewis, 2020; Kawamoto et al., 2022). In this case, the potential risk posed by an object or mission is evaluated either by assessing the average frequency with which such object is involved in collision events, as predicted by the simulations, or by looking at how differently the debris environment evolves with and without the spacecraft to be ranked.

This paper presents the *severity* term that has been formulated for the THEMIS (Track the Health of the Environment and Missions in Space) software (Colombo et al., 2021; Colombo et al., 2023) at Politecnico di Milano, in an ESA funded project carried out in collaboration with DEIMOS UK. The proposed metric is an extension of the index ECOB to any orbital region and dynamics. In particular, focus is here placed on the Medium-Earth Orbit (MEO), with the objective of ranking the in-orbit and future missions in this region. Effects maps are created over a suitable phase space of a subset of Keplerian elements to describe the consequence a fragmentation would have on the active satellites population, monitored in terms of cumulative collision probability with a set of representative target objects. A continuity equation-based model is adopted for the propagation of the simulated fragments clouds under the effect of the main orbital perturbations in MEO, i.e., second order zonal harmonic J_2, Solar Radiation Pressure (SRP), and luni-solar perturbation (Giudici et al., 2022; Giudici et al., 2023). As the computation of the severity term involves the characterisation of several debris clouds, the optimisation of the propagator performance is paramount. To this purpose, two crucial measures are taken. First, double averaged dynamics is employed to reduce the computation effort associated to the evaluation of the third-body acceleration. The effect of this modelling assumption on accuracy is analysed. Second, it is mathematically demonstrated how, in case of conservative forces, the divergence of the force field, which is needed for the density equation, does not require computing the second partial derivatives of the disturbing potential, considerably improving the overall efficiency. The effect of each simulated fragments cloud is evaluated through a flux-based collision risk model, directly from the debris density function (Letizia et al., 2016a; Frey and Colombo, 2021; Giudici et al., 2024). Effects maps of both satellite explosions and catastrophic collisions are computed against the 2023 active objects population. The currently in-orbit missions are eventually ranked according to the computed maps.

The paper is, next to the introduction, organised in four sections. Section 2 explains the modelling approach used for the propagation of fragments clouds in MEO and the evaluation of the collision probability with a target object. Section 3 describes the logic and the method adopted for the evaluation of the space environmental impact of a breakup in MEO. Section 4 presents the results obtained for the effects maps of both satellite explosions and catastrophic collisions against the active objects population in 2023. The currently in-orbit missions are ranked based on the computed maps. Section 5 draws the conclusions of the work.

2. Space debris cloud in medium-Earth orbit

This section presents the adopted approach for the modelling of a space debris cloud in medium-Earth orbit, which is used for the evaluation of the effect of a fragmentation in the same region, as detailed in Section 3. In particular, a synthetic fragmentation is followed throughout its lifetime,

assessing the fragments dispersion caused by the energy released by the breakup, the dynamical evolution of the cloud under the effect of the orbital perturbations, and the collision risk posed to a selected orbiting object. To this purpose, the density-based cloud propagation tool (Giudici et al., 2022; Giudici et al., 2023) and collision risk assessment method (Giudici et al., 2024), presented in previous works by the authors, are adopted.

The synthetic fragmentation considered in this section is a Galileo-like satellite explosion, arbitrarily triggered on 1st January 2024. The parent object Keplerian elements are reported in Table 1. Note that, as it is detailed in Section 3, the choice of setting a null fragmentation argument of latitude $u = \omega + f$ is made to guarantee the widest spread of the fragments over inclination (Giudici et al., 2023). Therefore, with the aim of determining the effect of a fragmentation event, it is identified as a worst-case scenario.

2.1. Density distribution at fragmentation epoch

The density distribution at fragmentation epoch is estimated through a probabilistic reformulation of the NASA Standard Breakup Model (SBM) (Johnson et al., 2001) in the 7D phase space of Keplerian elements and area-to-mass ratio (Frey and Colombo, 2021; Giudici et al., 2022). The model bounds the domain probabilistically reachable by the ejected fragments and computes the discretised phase space density function, which best resembles the actual fragments distribution. Fig. 1 shows the resulting density distribution as function of the slow-varying Keplerian elements (semi-major axis a, eccentricity e, inclination i, right ascension of the ascending node Ω, argument of perigee ω), and area-to-mass ratio A/M, considering fragments in the size range [1 cm, 1 m]. Instead, the dependency on the fast angular variable, either true anomaly f or mean anomaly M, is not here considered. Indeed, as the aim of this study is the assessment of the long-term effect of a potential fragmentation in MEO on the satellites population, the process of toroid formation, induced by the different orbital energy of the fragments, can be neglected as it takes place on a much shorter time scale. As a result, the fragments distribution is always assumed as randomised over mean anomaly M. For the results here presented, the scaling factor S, that determines the number of ejected fragments for explosion events according to the NASA SBM (Johnson et al., 2001), is arbitrarily set to 1. Note that this parameter only affects the number of generated debris from the breakup and not the shape of the distribution. Hence, the analysis on the fragments cloud evolution presented in the next sections maintains general validity.

Table 1
Galileo-like fragmentation Keplerian elements.

a [km]	e [-]	i [deg]	Ω [deg]	ω [deg]	f [deg]
29593	0.0	56.0	0.0	0.0	0.0

By looking at Fig. 1, a few considerations can be done:

- Because of the high specific orbital energy of the Galileo orbit, if compared to satellites in LEO, the velocity change given by the breakup causes the fragments to widely spread over the phase space. As a result, the fragments orbits show notable eccentricity values and cover a range as large as 2×10^4 km over semi-major axis. Note that, as the parent orbit is circular, a V-shaped distribution over the semi-major axis-eccentricity domain is observed.
- As the fragmentation is triggered at one of the orbital nodes, the fragments orbit inclination is considerably varied with respect to the parent one. On the contrary, as all fragments are constrained to share the same initial position, in correspondence of the parent orbit ascending node, no variation in right ascension of the ascending node Ω is observed.
- The particular shape of the fragments distribution in argument of perigee can be interpreted through simple geometric considerations. By looking at the plot in (a, ω), it turns out that the fragments orbits with the lowest (highest) semi-major axis values are characterised by $\omega \approx 180$ deg ($\omega \approx 0, 360$ deg). Indeed, such orbits have the apogee (perigee) in correspondence of the fragmentation point, that, for the considered fragmentation conditions, coincides with the ascending node for all the fragments orbits.

2.2. Debris cloud evolution

The density distribution of Fig. 1 is propagated in time through the numerical integration of the continuity equation with the Method Of Characteristics (MOC) (Jhon et al., 1981). The MOC discovers characteristic curves along which a Partial Differential Equation (PDE) transforms into a system of Ordinary Differential Equations (ODEs). For the continuity equation, the system of ODEs reads as:

$$\begin{cases} \frac{\mathrm{d}n}{\mathrm{d}t} = -n\nabla \cdot \boldsymbol{F} \\ \frac{\mathrm{d}\boldsymbol{y}}{\mathrm{d}t} = \boldsymbol{F} \end{cases} \tag{1}$$

where n is the phase space density, $\boldsymbol{y}$ the phase space variables, and $\boldsymbol{F}$ the orbital dynamics equations. The considered force model accounts for the Earth gravitational potential, described through spherical harmonics up to order 2 (i.e., Keplerian term and J_2 perturbation), SRP neglecting the effect of shadows, and Sun and Moon as disturbing bodies (Colombo, 2016). Atmospheric drag is not included, as none of the fragments is found to orbit at an altitude with relevant atmospheric density. As a result, the force model is conservative. The phase space variables $\boldsymbol{y}$ are the Keplerian elements γ and area-to-mass ratio A/M, which means that the dynamics equations can be conveniently obtained through the Lagrange Planetary Equa-

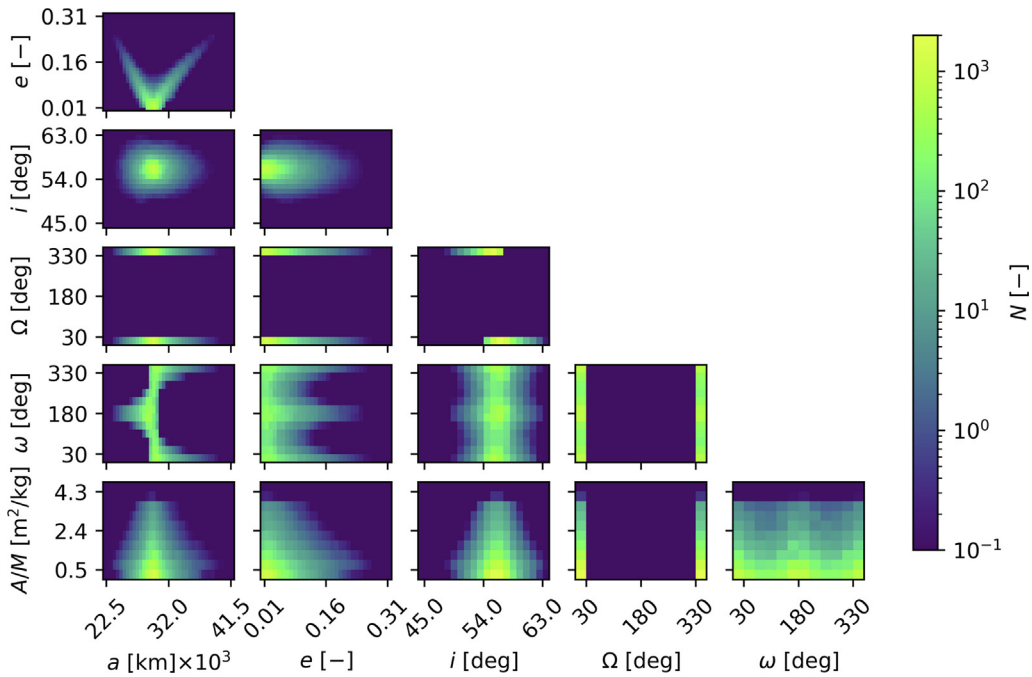

Fig. 1. Phase space density distribution as function of the slow-varying Keplerian elements and area-to-mass ratio, at fragmentation epoch. The colorbar depicts the total number of fragments in a bin in the two given variables, for any values of the other elements.

tions (LPEs) (Vallado and McClain, 2007). The LPEs express the time derivative of the Keplerian elements as the product between variable-dependent coefficients and the partial derivatives of the disturbing function $\mathscr{R}$ with respect to the Keplerian elements. They can be written in compact form as follows.

$$\frac{\mathrm{d}\gamma}{\mathrm{d}t} = \mathscr{C}(\gamma)\frac{\partial \mathscr{R}}{\partial \gamma}, \qquad \gamma := \{a, e, i, \Omega, \omega, M\} \tag{2}$$

where the matrix of coefficients $\mathscr{C}$ takes the form reported in Eq. (3).

$$\mathscr{C}(\gamma) = \begin{bmatrix} 0 & 0 & 0 & 0 & 0 & c_{aM}(a) \\ 0 & 0 & 0 & 0 & c_{e\omega}(a,e) & c_{eM}(a,e) \\ 0 & 0 & 0 & c_{i\Omega}(a,e,i) & c_{i\omega}(a,e,i) & 0 \\ 0 & 0 & c_{\Omega i}(a,e,i) & 0 & 0 & 0 \\ 0 & c_{\omega e}(a,e) & c_{\omega i}(a,e,i) & 0 & 0 & 0 \\ c_{Ma}(a) & c_{Me}(a,e) & 0 & 0 & 0 & 0 \end{bmatrix} \tag{3}$$

Note also that the following relation applies for the coefficients of the matrix $\mathscr{C}$ (Vallado and McClain, 2007):

$$c_{\gamma_1\gamma_2} = -c_{\gamma_2\gamma_1} \tag{4}$$

The density equation in Eq. (1) requires the evaluation of the divergence of the force field, which from Eq. (2) can be written as:

$$\nabla \cdot \boldsymbol{F} = \sum_{i=1}^{6}\sum_{j=1}^{6}\left(\frac{\partial c_{\gamma_i\gamma_j}}{\partial \gamma_i}\frac{\partial \mathscr{R}}{\partial \gamma_j} + c_{\gamma_i\gamma_j}\frac{\partial^2 \mathscr{R}}{\partial \gamma_i \partial \gamma_j}\right) \tag{5}$$

As the partial derivatives are independent of the order with which the differentiation is performed, i.e.:

$$\frac{\partial^2 \mathscr{R}}{\partial \gamma_i \partial \gamma_j} = \frac{\partial^2 \mathscr{R}}{\partial \gamma_j \partial \gamma_i} \tag{6}$$

Eq. (5) can be conveniently rearranged as follows.

$$\begin{aligned} \nabla \cdot \boldsymbol{F} = \; & \sum_{i=1}^{6}\sum_{j=1}^{6}\frac{\partial c_{\gamma_i\gamma_j}}{\partial \gamma_i}\frac{\partial \mathscr{R}}{\partial \gamma_j} + \sum_{i=1}^{6} c_{\gamma_i\gamma_i}\frac{\partial^2 \mathscr{R}}{\partial \gamma_i^2} \\ & + \sum_{i=1}^{6}\sum_{j=i+1}^{6}\left(c_{\gamma_i\gamma_j} + c_{\gamma_j\gamma_i}\right)\frac{\partial^2 \mathscr{R}}{\partial \gamma_i \partial \gamma_j} \end{aligned} \tag{7}$$

The second term is null as all the $c_{\gamma_i\gamma_i}$ coefficients are equal to zero. In addition, because of the property of the coefficients of the matrix $\mathscr{C}$ of Eq. (4), and since each $c_{\gamma_1\gamma_2}$ coefficient has its correspondent inverse $c_{\gamma_2\gamma_1}$, also the third term of Eq. (7) nullifies, yielding to the following expression for the divergence of a conservative force field:

$$\begin{aligned} \nabla \cdot \boldsymbol{F} = \; & \frac{\partial c_{i\Omega}}{\partial i}\frac{\partial \mathscr{R}}{\partial \Omega} + \left(\frac{\partial c_{e\omega}}{\partial e} + \frac{\partial c_{i\omega}}{\partial i}\right)\frac{\partial \mathscr{R}}{\partial \omega} \\ & + \left(\frac{\partial c_{aM}}{\partial a} + \frac{\partial c_{eM}}{\partial e}\right)\frac{\partial \mathscr{R}}{\partial M} \end{aligned} \tag{8}$$

Therefore, the computation of the divergence term does not require the evaluation of the second partial derivatives of the disturbing function with respect to the Keplerian elements, considerably improving the computational efficiency. Note also that if the disturbing function were independent of Ω, ω and M, the divergence of $\boldsymbol{F}$ would nullify and the phase space density would be conserved along the characteristic curves.

The dynamics equations considered within this work are averaged over the fast angular variable, as evaluating the short-term effect of orbital perturbation is outside the scope of this study. In addition, as decreasing the compu-

tational cost associated to the propagation is crucial for the computation of the effects map (Section 4), due to the considerable number of fragmentation events to be characterised, a double average formulation of the third-body potential is preferred. In the following, the averaged disturbing potentials for all the considered perturbations are shortly summarised.

2.2.1. Geopotential model

Earth gravitational potential $U_\oplus$ is typically modelled as a sum of harmonics, as follows (Vallado and McClain, 2007).

$$U_\oplus = -\frac{\mu_\oplus}{r}\left[1+\sum_{n=2}^{N_z}\frac{J_n P_n^0(\sin\phi)}{\left(\frac{r}{R_\oplus}\right)^n} + \sum_{n=2}^{N_t}\sum_{m=1}^{n}\frac{P_n^m(\sin\phi)\left(C_n^m\cos m\lambda + S_n^m\sin m\lambda\right)}{\left(\frac{r}{R_\oplus}\right)^n}\right] \tag{9}$$

where $\mu_\oplus$ and $R_\oplus$ are the Earth gravitational parameter and mean radius, r is the object orbital radius, λ and ϕ are its longitude and latitude, respectively, P_n^0 are the Legendre polynomials and P_n^m the associated Legendre functions, and J_n, C_n^m and S_n^m are coefficients. Excluding the Keplerian component $\mu_\oplus/r$, the dominating term in $U_\oplus$, and the only one modelled within this study, is provided by the J_2 coefficient, which represents the disturbing effect induced by the oblateness of the Earth. Therefore, the following disturbing function is here considered (Vallado and McClain, 2007):

$$\mathscr{R}_{J_2} = \frac{\mu_\oplus J_2 R_\oplus^2}{2r^3}\left(3\sin^2\phi - 1\right) \tag{10}$$

To filter out the short-term effects, the disturbing function $\mathscr{R}_{J_2}$ is averaged over mean anomaly M, as follows (Vallado and McClain, 2007).

$$\overline{\mathscr{R}}_{J_2} = \frac{1}{2\pi}\int_0^{2\pi}\mathscr{R}_{J_2}\frac{\mathrm{d}M}{\mathrm{d}f}\,\mathrm{d}f = \frac{J_2 R_\oplus^2}{4}\frac{n^2\left(3\sin^2 i - 2\right)}{\left(1-e^2\right)^{3/2}} \tag{11}$$

with n mean motion. As expected, the averaged oblateness disturbing potential $\overline{\mathscr{R}}_{J_2}$ does not depend on right ascension of the ascending node Ω, argument of perigee ω, and mean anomaly M, which means that semi-major axis a, eccentricity e, and inclination i keep constant on the long term. Note also that, according to Eq. (8), the component of the divergence of the force field associated to the J_2 perturbation is identically null, meaning that Earth oblateness does not cause any long-term variation of the phase space density.

2.2.2. Solar radiation pressure model

Neglecting shadowing effects, SRP is conservative and can be described through the following disturbing potential (Vallado and McClain, 2007):

$$\mathscr{R}_{\mathrm{SRP}} = p_{\mathrm{SRP}}\, c_r \frac{A}{M} X \tag{12}$$

where $p_{\mathrm{SRP}} = 4.56\times10^{-6}$ N/m^2 is the solar pressure at 1 AU, c_R is the reflectivity coefficient of the impacted object, A/M its area-to-mass ratio, and X is the coordinate of the object in an Earth-centered rotating reference frame with the x-axis pointing towards the Sun. X can be written as function of the orbital elements through the following relation:

$$X = [1,0,0]\,R_3(\lambda_\odot)R_1(\varepsilon)R_3(-\Omega)R_1(-i)R_3(-u)\begin{bmatrix} r \\ 0 \\ 0 \end{bmatrix} \tag{13}$$

with R_1 and R_3 rotation matrices around x-axis and z-axis, respectively, $\lambda_\odot$ longitude of the Sun, ε obliquity of the ecliptic plane, and $u = \omega + f$ object argument of latitude. The integral average of Eq. (12) over mean anomaly M yields the averaged disturbing potential of the SRP perturbation, whose expression is not reported here for brevity and can be found in Gkolias et al. (2020).

2.2.3. Third-body potential model

If the distance Earth-object is significantly smaller than the Earth-third body one, the third-body disturbing function $\mathscr{R}_{3B}$ can be written as a series expansion in the parallactic ratio $\delta = a/r_{3B}$, as follows (Vallado and McClain, 2007).

$$\mathscr{R}_{3B} = \frac{\mu_{3B}}{r_{3B}}\sum_{k=2}^{\infty}\delta^k\left(\frac{r}{a}\right)F_k(\cos\psi) \tag{14}$$

where μ_{3B} and r_{3B} are the third-body gravitational parameter and orbital radius, respectively, and ψ is the angle between the object and third-body position vectors measured from Earth. This latter can be expressed according to the following relation:

$$\cos\psi = \frac{\boldsymbol{r}\cdot\boldsymbol{r}_{3B}}{r r_{3B}} = \hat{\boldsymbol{r}}\cdot\hat{\boldsymbol{r}}_{3B} \tag{15}$$

To isolate the dependency on the fast angular variable, the unit vector $\hat{\boldsymbol{r}}$ is expressed as in Kaufman and Dasenbrock (1972, 1973):

$$\hat{\boldsymbol{r}} = \hat{\boldsymbol{P}}\cos f + \hat{\boldsymbol{Q}}\sin f \tag{16}$$

with $\hat{\boldsymbol{P}}$ and $\hat{\boldsymbol{Q}}$ eccentricity and semilatus rectum unit vectors, respectively. For the results presented in this work, the series expansion in Eq. (14) is truncated at the second order. Again, this choice comes as a compromise between accuracy and computational cost. The averaged disturbing function, truncated at order 2, takes the following form (Kaufman and Dasenbrock, 1972; Kaufman and Dasenbrock, 1973):

$$\overline{\mathscr{R}}_{3B} = \tfrac{1}{4}\tfrac{\mu_{3B}}{r_{3B}}\delta^2\left[3A_{3B}^2(4e^2+1) + 3B_{3B}^2(1-e^2) - 3e^2 - 2\right] \tag{17}$$

with A_{3B} and B_{3B} defined as (Colombo, 2019):

$$A_{3B} = \hat{\boldsymbol{P}} \cdot \hat{\boldsymbol{r}}_{3B}$$
$$B_{3B} = \hat{\boldsymbol{Q}} \cdot \hat{\boldsymbol{r}}_{3B} \tag{18}$$

As already commented, besides the single averaged formulation of the third-body potential, this paper investigates the feasibility of performing a second averaging of the potential over the third-body mean anomaly. Indeed, when the luni-solar perturbation becomes significant, it notably affects the computational cost associated to the cloud propagation, considerably decreasing the integration step and, consequently, increasing the number of function evaluations. The slower dynamics are expected to relax the constraint on the integration step, but analyses are required to verify whether the simplified dynamics guarantees a sufficient accuracy for the purpose of this study. To highlight the dependency of $\overline{\mathscr{R}}_{3B}$ on the anomaly of the third-body, r_{3B} is expressed as in Eq. (16). Therefore, Eq. (18) modifies as:

$$A_{3B} = c_{11} \cos f_{3B} + c_{12} \sin f_{3B}$$
$$B_{3B} = c_{21} \cos f_{3B} + c_{22} \sin f_{3B} \tag{19}$$

with $c_{11} = \hat{\boldsymbol{P}} \cdot \hat{\boldsymbol{P}}_{3B}$, $c_{12} = \hat{\boldsymbol{P}} \cdot \hat{\boldsymbol{Q}}_{3B}$, $c_{21} = \hat{\boldsymbol{Q}} \cdot \hat{\boldsymbol{P}}_{3B}$, and $c_{22} = \hat{\boldsymbol{Q}} \cdot \hat{\boldsymbol{Q}}_{3B}$. The integral average of Eq. (17) leads to the double average expression of the third-body disturbing function (Colombo, 2019):

$$\begin{aligned}\overline{\overline{\mathscr{R}}}_{3B} &= \frac{n_{3B}^2 a^2}{8(1-e_{3B})^{3/2}}\left[-2(2+3e^2)\right.\\ &\left.+3(4e^2+1)\left(c_{11}^2+c_{12}^2\right)+3(1-e^2)\left(c_{21}^2+c_{22}\right)\right]\end{aligned} \tag{20}$$

The density distribution depicted in Fig. 1 is propagated in time through the MOC, according to the described force model. Ten thousand characteristics are uniformly sampled from the portion of the phase space occupied by the cloud at fragmentation epoch, and the variation of coordinates and density is retrieved from the numerical integration of Eq. (1). The propagated characteristics are eventually interpolated through binning in the 6D phase space of slow-varying Keplerian elements and area-to-mass ratio (Giudici et al., 2023), at specified time epochs. Therefore, the computed debris density discretely varies over both phase space and time. Fig. 2 shows the resulting fragments distribution 1, 5, 10 and 15 years after fragmentation.

Understanding the dynamical evolution of a cloud of fragments is a complex task, as the ejected debris vastly spread out over the phase space, as a consequence of the considerable impulse they receive from the fragmentation. As a result, fragments are found to orbit in very different orbital regimes, e.g., circular MEO and considerably eccentric orbits. In addition, at the altitude of the modelled fragmentation, the considered orbital perturbations significantly affect the objects dynamics, and their coupled effect may induce resonant behaviour (Rossi, 2008; Skoulidou et al., 2019). The most observable changes are monitored in inclination i, right ascension of the ascending node Ω, and argument of perigee ω. As the magnitude of the J_2 perturbation strongly depends on the distance from Earth, the fragments on the left-hand leg of the distribution in (a, e) experience more remarkable changes in Ω and ω, if compared to the right-hand leg. By looking at the fragments evolution in inclination, it can be seen that a bifurcation appears for the objects with apogee radius greater than the fragmentation orbital radius, induced by a more significant decrease in inclination for fragments on initially less inclined orbits. This behaviour is induced by the coupled effect of J_2 and Moon perturbations.

To verify the validity of the double average formulation of the third-body disturbing function of Eq. (20), each sample is propagated considering both the single- and double-averaged potentials, monitoring the maximum error in eccentricity e and inclination i throughout the propagation time. The results are shown in Fig. 3. The left-hand figures depict the maximum variations in e and i over the propagation period, while the right-hand figures the associated absolute maximum error. For both the elements, the accuracy degradation introduced by the doubly-averaged potential is sufficiently small, with the absolute error that remains two orders of magnitude lower than the maximum variation in the two variables. An extensive validation of the double average dynamics in MEO can be found in Pellegrino et al. (2022).

2.3. Collision probability with a single object

The collision probability is modelled as a Poisson distribution (McKnight, 1990; Chobotov, 1991). Defined as η the cumulative number of impacts between a fragments cloud and a target object, the probability of having at least one collision in $t \in [0, \tilde{t})$ is computed as:

$$P_c(\tilde{t}) = 1 - \exp\left[-\eta(\tilde{t})\right] \tag{21}$$

where η can be obtained from the impact rate $\dot{\eta}$ through integration as:

$$\eta(\tilde{t}) = \int_0^{\tilde{t}} \dot{\eta}(t, A_c)\,\mathrm{d}t \tag{22}$$

The impact rate is retrieved through the computation of the fragments flux against the target object cross-sectional area A_c, from the debris density function in Keplerian elements n (Frey and Colombo, 2021; Giudici et al., 2024). As commented in Section 2.2, the fragments distribution is here modelled as a discrete function of time, meaning that if N_t is the number of time intervals considered, and Δt_i the associated time steps, the integral of Eq. (22) can be transformed into a summation as follows.

$$\eta(\tilde{t}) = \sum_{i=1}^{N_t-1} \frac{\dot{\eta}_i + \dot{\eta}_{i+1}}{2} \Delta t_i \tag{23}$$

with $\dot{\eta}_i$ and $\dot{\eta}_{i+1}$ impact rates evaluated at the extrema, t_i and t_{i+1}, of each time interval Δt_i. As the collision rate is discretely computed over time, with a frequency much lower than the frequency of revolution of the object around

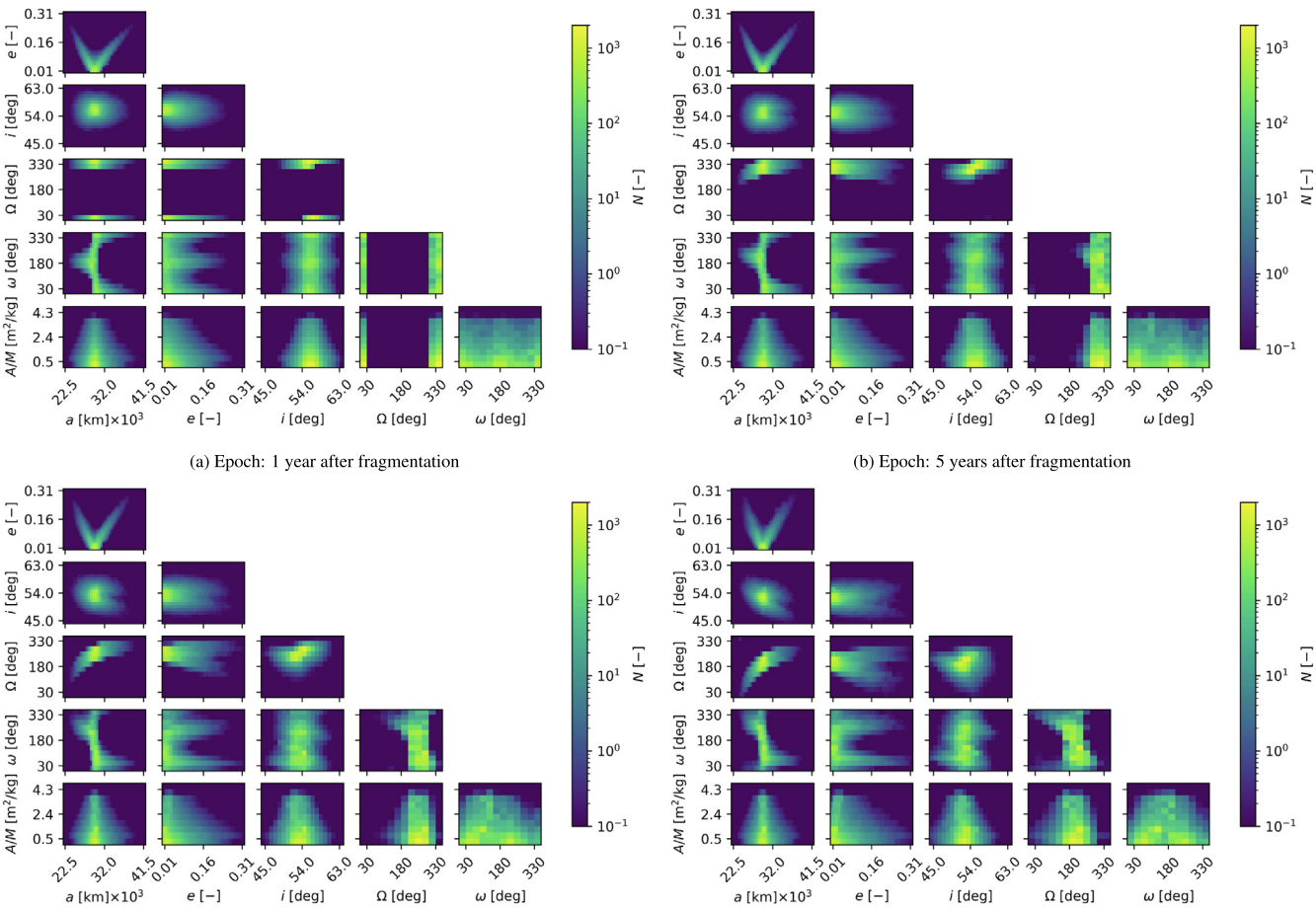

(a) Epoch: 1 year after fragmentation

(b) Epoch: 5 years after fragmentation

(c) Epoch: 10 years after fragmentation

(d) Epoch: 15 years after fragmentation

Fig. 2. Phase space density distribution in the slow-varying Keplerian elements and area-to-mass ratio over time.

the Earth, it is reasonable to compute an average impact rate over an entire intact object orbit rather than for a unique position along it. Defined as $\boldsymbol{r}_T(t), \boldsymbol{v}_T(t)$ the position and velocity vectors of the target object, respectively, and T_T its orbital period, the averaged impact rate at a generic time t_i reads as:

$$\dot{\eta}_i = \frac{1}{T_T} \int_0^{T_T} \dot{\eta}(n(t_i), \boldsymbol{r}_T(t), \boldsymbol{v}_T(t), A_c)\, \mathrm{d}t \tag{24}$$

Note that the density n is constant over one period T_T. On the contrary, since the object evolves along its Keplerian orbit, the intersection conditions between fragments and target orbit vary and, as a consequence, the relative velocity of impact is a function of time. Full detail on the theory for the evaluation of the impact rate from the density function n is not reported here for brevity but it can be found in Giudici et al. (2024).

The collision risk model is adopted in this section for the estimation of the impact rate and collision probability with two Galileo-like satellites, to observe the potential threat that a breakup may pose on satellites in the same constellation as the parent object. The first selected target orbit coincides with the parent one, while the second is shifted of 180 deg in right ascension of the ascending node. The same cross-sectional area of 3.24 m^2 is considered for the two objects. The resulting profiles of the impact rate and cumulative collision probability over time are displayed in Fig. 4.

To understand the profiles of Fig. 4, let us consider the spatial distribution of the fragments with respect to the target orbits. The spatial distributions 1, 8 and 15 years after fragmentation are shown in Fig. 5. As it can be inferred, the highest impact rate is monitored when the target orbit is shifted in right ascension of the ascending node of 180 deg with respect to the main bulk of debris. On the contrary, when the target orbital plane is similar to fragments one, the impact rate is the lowest, as it is the case of the first target within the first year of simulation. Indeed, it must be considered that in this second scenario, even though the target object is continuously surrounded by the fragments as it moves along its orbit, the relative velocity of impact is relatively small, inducing a notably lower flux. As a result, since the cloud performs almost half a revolution in right ascension of the ascending node over the

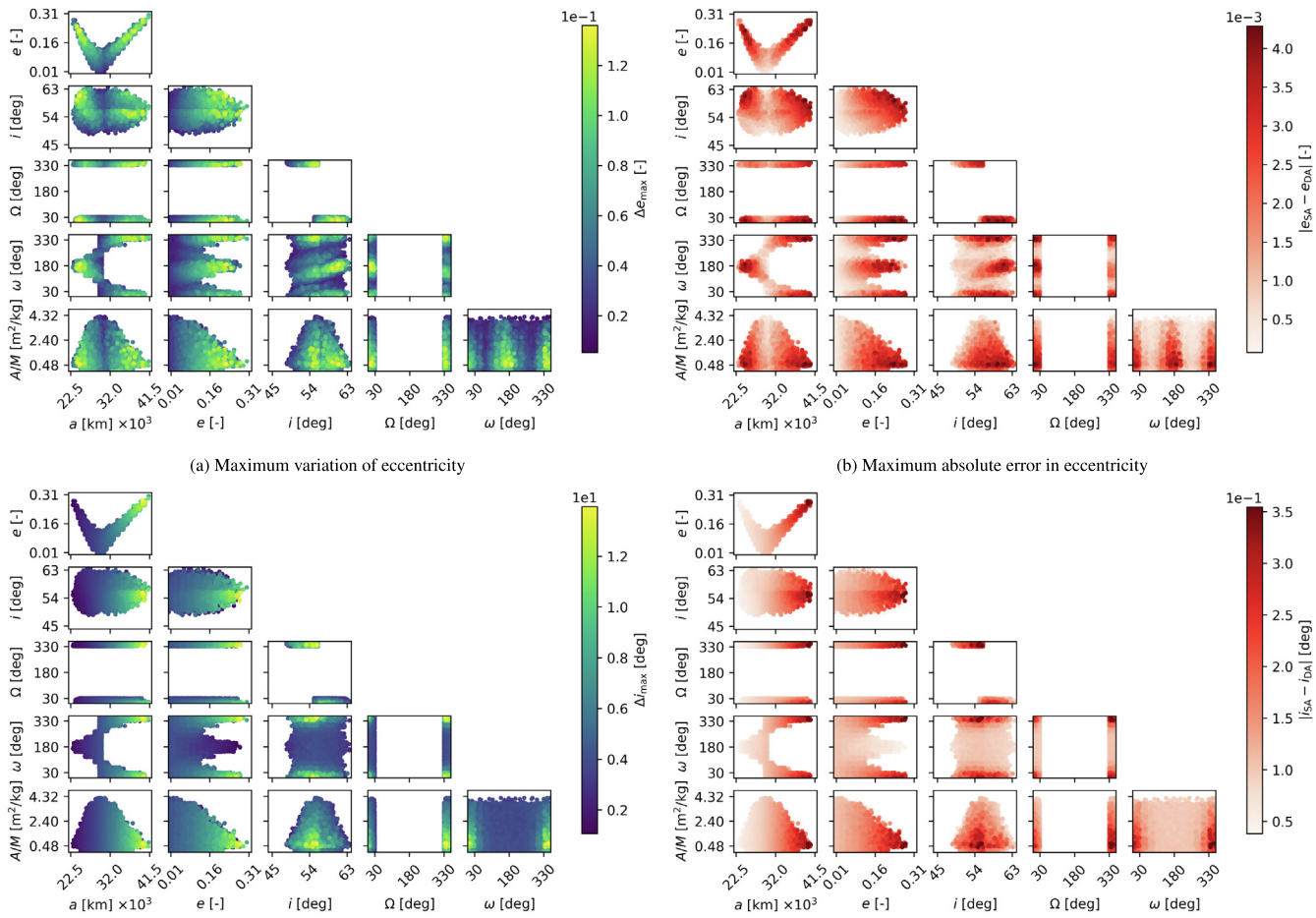

(a) Maximum variation of eccentricity

(b) Maximum absolute error in eccentricity

(c) Maximum variation of inclination

(d) Maximum absolute error in inclination

Fig. 3. Comparison between single and double average formulations of the third-body potential.

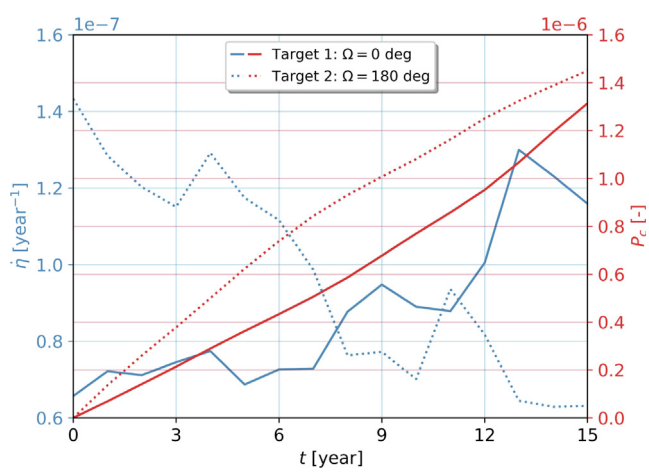

Fig. 4. Impact rate and cumulative collision probability over time.

studied time frame, the impact rate profiles are nearly symmetric.

3. Effects map computation workflow

This section is devoted to explaining the logic and the methodology adopted for the evaluation of the space environmental impact of a breakup in MEO. The approach proposed in this paper is an extension of the ECOB formulation developed in Letizia et al. (2016b, 2017). The idea is to assign an effect value to an object or mission, based on the collision risk posed by its potential breakup to the active satellites population. The reason why this sustainability metric is attractive is that it provides a direct and easily understandable measure of the consequences of a fragmentation in terms of potential loss for the spacecraft operators.

The tool used to assign a breakup severity value to a mission is called effects map. It is a representation of the medium-Earth orbital region over a properly defined phase space, displaying the cumulative impact probability of the fragments cloud generated by the object breakup with the satellites in the same region, as function of the map variables. As detailed in the next sections, the active satellites

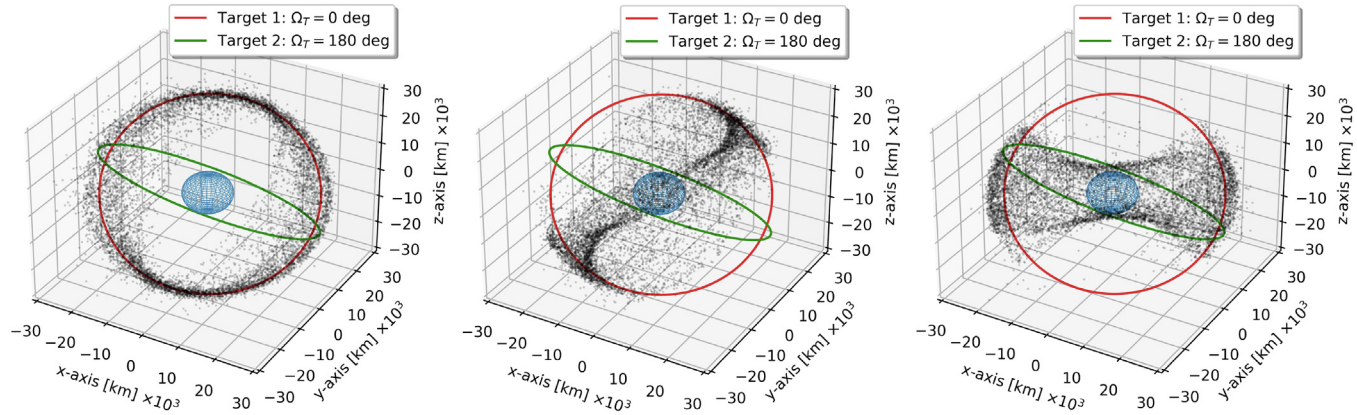

(a) Epoch: 1 year after fragmentation (b) Epoch: 8 years after fragmentation (c) Epoch: 15 years after fragmentation

Fig. 5. Fragments spatial distribution with respect to the targets orbit.

population is translated into a set of representative targets. The selection of the optimal set of phase space variables for the computation of the effects map in MEO is then addressed. A grid of fragmentations is defined over the selected phase space, and for each cell a satellite explosion and a catastrophic collision are triggered, and the resulting clouds propagated. The effect term for each fragmentation type and location is computed based on the cumulative collision probability with the representative targets population, over a defined time frame.

3.1. Representative targets of the active satellites population

The population of active satellites in MEO is retrieved from the DISCOS Database (Database and Information System Characterising Objects in Space) (McLean et al., 2017). The spacecraft are gathered into a set of representative targets according to a grid in a subset of Keplerian elements. The choice of the grid variables is made by identifying the elements which are most functional to the characterisation of the objects distribution in the considered region. The objective of this procedure is the limitation of the computational effort, as it allows the evaluation of the collision probability with a limited number of fictitious objects only, which are representative of the overall satellites population. Semi-major axis a, inclination i, and right ascension of the ascending node Ω are identified as the best variables for the description of the spacecraft currently in orbit in the MEO region. The ranges and step-sizes of the considered grid are reported in Table 2. Eccentricity and argument of perigee are not included as relevant variables because of the predominant use of circular orbits in MEO. Hence, they are both arbitrarily set to zero.

Table 2
Grid ranges and step-sizes for the selection of the representative targets.

	a [km]	i [deg]	Ω [deg]
Lower limit	12000	0.0	0.0
Upper limit	32000	90.0	360.0
Step-size	500	5.0	60.0

To further limit the computational load, a pruning of the representative targets, based on their cumulative cross-sectional area (i.e., the sum of the areas of the objects of which the target is representative), is performed. Indeed, one must remember that this property directly impacts on the collision probability and, thus, on the severity term. For the results presented in this work, only the representative targets with a cumulative cross-sectional area greater than 25 m^2 are considered (Muciaccia et al., 2023).

For each representative target, information on the average and cumulative cross-sectional area is needed. Indeed, the first is adopted for the actual computation of the impact probability, as it is representative of the *average* satellite in that location. Instead, the cumulative area is used to weight the collision risk value for each target object relative to the others. Fig. 6 depicts the representative targets' average, $\overline{A_c}$, and cumulative, A_c^{tot}, cross-sectional areas as function of semi-major axis, inclination, and right ascension of the ascending node, obtained from the 2023 active objects population. The orbital and physical parameters of the targets are also listed in Table 3.

3.2. Map variables and discretisation

The same grid variables and discretisation adopted for the definition of the representative targets are used to trigger the fragmentations. Note that the reasoning behind the definition of the map variables is not only related to the objects distribution, but also to the effect such variables have on the fragments dynamics. For example, the right ascension of the ascending node, which was not included in the works on the ECOB index in LEO, has in MEO a fundamental role. Indeed, it has to be kept in mind that the orientation of the orbital plane significantly impacts on the orbital evolution of the objects in MEO, which are strongly affected by the coupled effect of J_2, luni-solar and SRP perturbations. Again, eccentricity and argument

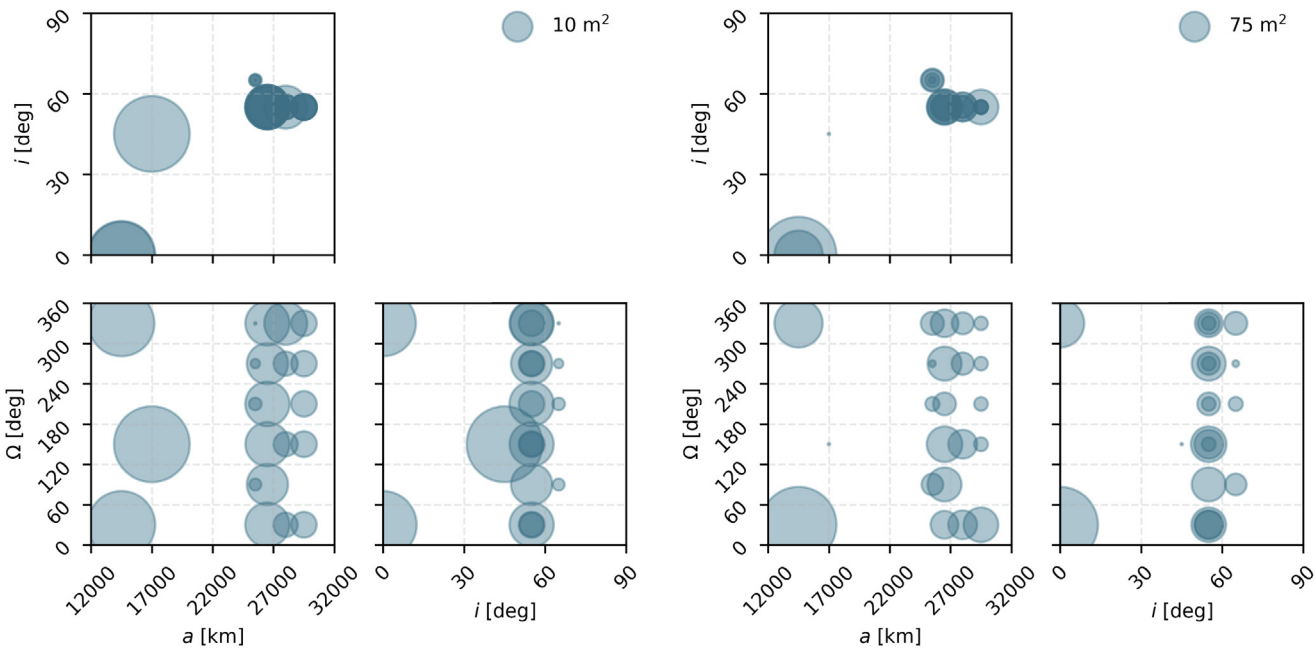

(a) Average (b) Cumulative

Fig. 6. Representative targets average and cumulative cross-sectional area as function of semi-major axis, inclination, and right ascension of the ascending node, from the 2023 active objects population in medium-Earth orbit.

Table 3
Parameters of the targets representative of the 2023 active objects population in medium-Earth orbit.

ID	a [km]	i [deg]	Ω [deg]	$\overline{A_c}$ [m^2]	A_c^{tot} [m^2]
1	14500	10^{-3}	30.0	22.70	340.54
2	14500	10^{-3}	330.0	21.98	153.86
3	17000	45.0	150.0	26.84	26.84
4	25500	65.0	90.0	7.44	52.11
5	25500	65.0	210.0	7.49	37.45
6	25500	65.0	270.0	7.25	28.99
7	25500	65.0	330.0	6.96	55.69
8	26500	55.0	30.0	13.73	68.64
9	26500	55.0	90.0	12.85	89.92
10	26500	55.0	150.0	13.67	95.72
11	26500	55.0	210.0	13.74	55.00
12	26500	55.0	270.0	12.83	89.82
13	26500	55.0	330.0	13.71	68.54
14	28000	55.0	30.0	8.98	71.88
15	28000	55.0	150.0	8.98	71.88
16	28000	55.0	270.0	8.98	53.91
17	28000	55.0	330.0	13.32	53.27
18	29500	55.0	30.0	9.24	92.37
19	29500	55.0	150.0	9.26	37.03
20	29500	55.0	210.0	9.22	36.89
21	29500	55.0	270.0	9.22	36.89
22	29500	55.0	330.0	9.22	36.89

of perigee are not included as the vast majority of the missions in MEO use circular orbits (e.g., navigation satellites constellations).

By looking at the representative targets distribution in MEO as function of semi-major axis, displayed in Fig. 6, it can be observed that the missions currently in-orbit gather in two main regions, a low-altitude one at $a \in [12000 - 17000]$ km and a high-altitude one at $a \in [25000 - 30000]$ km. Therefore, with the objective of reducing the computational cost, the effect term is evaluated for these two regions only, and the outcome is shown in two separate effects maps. This results in a total of 3420 fragmentations to be modelled for each fragmentation type.

According to the selected map phase space, the parent orbit semi-major axis a, inclination i, and right ascension of the ascending node Ω vary as specified by the fragmentation grid, while the remaining three Keplerian elements are user-defined and kept fixed. For the results here proposed the following choices were made:

- Eccentricity is set to zero, as most of the objects are on circular orbits.
- Argument of perigee is arbitrarily set to zero. Again, its definition has no effect on the results, as it is undefined for circular orbits.
- To characterise the worst-case scenario, true anomaly is set to zero, as it ensures a wider dispersion of the fragments over inclination.

3.3. Effect term

For each cell of the 3D grid in semi-major axis, inclination, and right ascension of the ascending node, two fragmentations are triggered: a satellite explosion and a catastrophic collision. The object breakup is modelled as explained in Section 2.1, with the fragments density charac-

terised over the phase space of slow-varying orbital elements and area-to-mass ratio. The initial distributions are sampled and propagated through the MOC for a user-defined time period, according to the dynamical model presented in Section 2.2. Fragments clouds resulting from collisions and explosions have different characteristics (Giudici et al., 2023). The former normally generate a vast population of very small fragments with high relative velocities, which induces the cloud to spread out over a much wider domain. Therefore, with the aim of modelling the two events with the same accuracy, a larger population of characteristics is propagated for the collision scenario. Explosion clouds are propagated along ten-thousand characteristic lines, while collisions along twice this number. The impact rate against the representative targets population is evaluated with a 1-year time discretisation from the fragments density in Keplerian elements, and the cumulative collision probability is evaluated according to Eqs. (21) and (23). The effect term is formulated as proposed in Letizia et al. (2016b): defined as $\overline{A_{ci}}, A_{c_i}^{\text{tot}}$ the average and total cross-sectional area of the ith representative target, and N_{rt} the total number of targets, the effect value of a fragmentation event with coordinates (a_k, i_k, Ω_k) is:

$$e_{\text{exp./coll.}} = \frac{\sum_{i=1}^{N_{rt}} P_c\left(a_k, i_k, \Omega_k, \overline{A_{ci}}\right) A_{c_i}^{\text{tot}}}{\sum_{i=1}^{N_{rt}} A_{c_i}^{\text{tot}}} \tag{25}$$

with the effect of the explosion, $e_{\text{exp.}}$, and the collision, $e_{\text{coll.}}$, computed from the related fragmentation clouds. It is worth commenting that the effect term is evaluated for a unique value of scaling factor S, for explosions, and fragmenting mass M, for collisions. Indeed, according to the NASA SBM, these parameters only affect the number of generated fragments, but not the distribution (Johnson et al., 2001). If the estimated number of impacts between a target object and the fragments, η, is of the order 10^{-2} or lower, which is a considerably high value in debris analyses, the collision probability of Eq. (21) is nearly coincident with η. Hence, as η linearly varies with the number of fragments, so does the value of the effect. Therefore, the effect scales with the scaling factor or the object mass the same way the number of fragments does, i.e. (Letizia et al., 2016b):

$$\begin{aligned} e_{\text{exp.}} &= \tfrac{S}{S_{\text{ref}}} e_{\text{exp.}}(S_{\text{ref}}) \\ e_{\text{coll.}} &= \left(\tfrac{M}{M_{\text{ref}}}\right)^{0.75} e_{\text{coll.}}(M_{\text{ref}}) \end{aligned} \tag{26}$$

with S_{ref} and M_{ref} reference scaling factor and mass, respectively, with which the effects maps are computed.

4. Effects map in medium-Earth orbit

This section presents the results obtained on the maps of the effects of both in-orbit catastrophic collisions and explosions on the targets representative of the 2023 active objects population in MEO. The two identified altitude regions are treated separately, because of the notable difference in the active objects distribution and, thus, in the expected behaviour of the effect term as function of the map variables. The results presented here consider a reference scaling factor S_{ref} equal to unity and a reference mass M_{ref} of 10000 kg.

The dependency of the severity of a fragmentation on the breakup coordinates is depicted through heatmaps in the three orbital elements defined in Section 3.2: semi-major axis a, inclination i, and right ascension of the ascending node Ω. As the effect is evaluated according to a three-dimensional grid, in order to visualise its behaviour, the 3D array of effect values is reduced to three 2D maps in $(a, i), (a, \Omega)$ and (i, Ω), where one of the dimensions is removed through averaging. The resulting maps represent the cumulative increment in collision probability that a fragmentation with the specified coordinates would cause to the active objects population in MEO. Hence, they provide a measure of the risk posed by a potential mission in that location to safe in-orbit operations.

For a better understanding of the results, the position of the representative targets, defined according to the methodology explained in Section 3.1, is displayed on top of the heatmaps.

4.1. Low-altitude region

Fig. 7 shows the effects maps for the low-altitude region of both explosions and catastrophic collisions.

As it can be inferred, since catastrophic collisions generate a much larger population of fragments with respect to explosions, according to the NASA SBM, they pose a higher risk to the orbiting objects in the same region, resulting in higher effect value. In addition, because of a greater average relative velocity with which the fragments are ejected in case of a collision, the gradient of the effect with respect to the map variables is lower. In other words, although fragmentations generated in the same altitude slot where a target object moves pose the highest risk, collisions occurring far from it could still cause a considerable threat to its safe operations. For both the maps, the effect term is mainly shaped by the representative targets at zero inclination and semi-major axis of 14500 km, where the absolute maximum is found. Note that the effect value decreases of one order of magnitude when moving from the cells at $i = 0$ deg to the ones at $i = 5, 10$ deg. When further increasing inclination, the risk grows at a very slow rate.

To justify this behaviour, let us perform a qualitative analysis on the collision risk posed to an equatorial target object by a fragmentation as function of the parent orbit inclination. The impact rate between fragments and target object takes the following general form:

$$\dot{\eta} = A_c\, n_{\boldsymbol{r}}(\boldsymbol{r}_T)\, v_{\text{rel}} \tag{27}$$

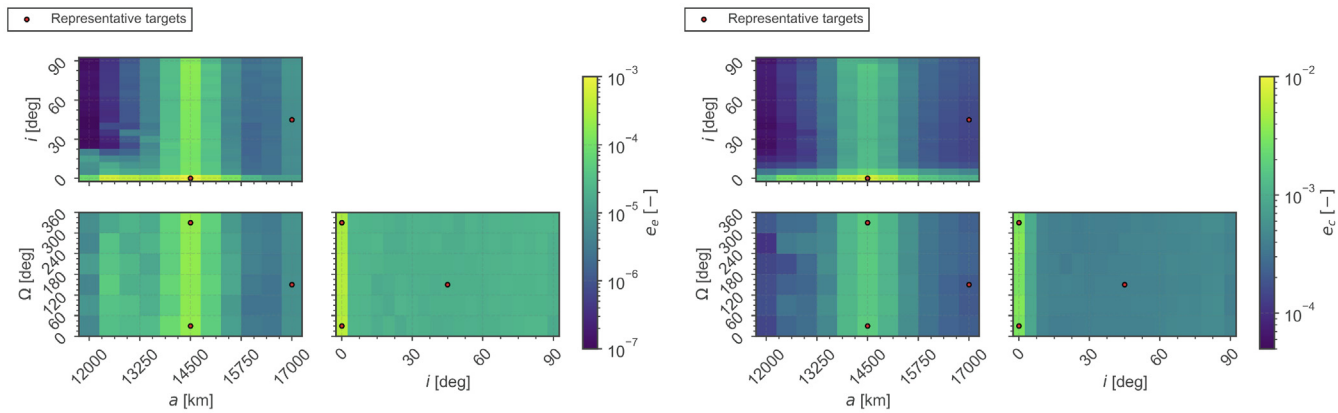

(a) Satellite explosions (b) Catastrophic collisions

Fig. 7. Effects maps in low-altitude MEO against the active objects population in the same region.

with n_r fragments spatial density. The spatial density can be expressed as the number of fragments $\mathrm{d}N$ in an infinitesimal volume $\mathrm{d}V$, i.e.:

$$n_r = \frac{\mathrm{d}N}{\mathrm{d}V} \tag{28}$$

The infinitesimal number of fragments $\mathrm{d}N$ can be split into a summation of terms $\mathrm{d}N_j$, which indicate the contribution of all possible fragments orbits intersecting the target object one, as follows.

$$n_r = \frac{\sum_j \mathrm{d}N_j}{\mathrm{d}V} \tag{29}$$

Considering orbital radius r, longitude λ, and latitude ϕ as spatial coordinates, the infinitesimal number of fragments $\mathrm{d}N_j$ in $\mathrm{d}V$, characterised by the same orbit, can be computed as:

$$\mathrm{d}N_j = N_j \frac{\mathrm{d}M}{2\pi} = \frac{N_j}{2\pi}\frac{\mathrm{d}M}{\mathrm{d}f}\left(\frac{\partial f}{\partial r}\mathrm{d}r + \frac{\partial f}{\partial \phi}\mathrm{d}\phi\right) \tag{30}$$

Note that, since the fragments N_j share the same orbit, only one between λ and ϕ is an independent variable. In Eq. (30), and for the derivation here proposed, the latitude ϕ is chosen as the independent one. As the objective is to analyse the dependency of the effect term on inclination, let us assume all intersecting fragments orbits as circular. Under this condition, Eq. (30) simplifies as follows.

$$\mathrm{d}N_j = \frac{N_j}{2\pi}\frac{\partial f}{\partial \phi}\mathrm{d}\phi \tag{31}$$

Indeed, neither the mean anomaly M nor the orbital radius r depend on true anomaly f. The relation between true anomaly and latitude ϕ is provided by spherical trigonometry and reads as:

$$\sin\phi = \sin f \sin i \tag{32}$$

from which it follows that:

$$\frac{\partial f}{\partial \phi} = \frac{\cos\phi}{\sqrt{\sin^2 i - \sin^2\phi}} \tag{33}$$

Therefore, the infinitesimal number of fragments $\mathrm{d}N_j$ in $\mathrm{d}V$ on an orbit with inclination i_j, can be written as:

$$\mathrm{d}N_j = \frac{N_j}{2\pi}\frac{\cos\phi}{\sqrt{\sin^2 i_j - \sin^2\phi}}\mathrm{d}\phi \tag{34}$$

The infinitesimal volume $\mathrm{d}V$ takes the following form:

$$\mathrm{d}V = 2\pi r^2 \cos\phi\,\mathrm{d}r\,\mathrm{d}\phi \tag{35}$$

Plugging Eq. (34) and Eq. (35) into Eq. (29), the spatial density can be expressed as follows.

$$n_r(r,\phi) = \sum_j \frac{N_j}{4\pi^2 r^2\,\mathrm{d}r}\frac{1}{\sqrt{\sin^2 i_j - \sin^2\phi}} \tag{36}$$

For the computation of the impact rate of Eq. (27), the spatial density has to be evaluated at the target coordinates, i.e., $r = r_T, \lambda = \lambda_T$, and $\phi = 0$ deg. It can be computed as follows.

$$n_r(r_T,\lambda_T,\phi_T) = \sum_j \begin{cases} \frac{N_j}{4\pi^2 r_T^2\,\mathrm{d}r}\frac{1}{\sin i_j} & \text{if } \Omega_j = \lambda_T \\ 0 & \text{otherwise} \end{cases} \tag{37}$$

with Ω_j right ascension of the ascending node of the jth orbit. Note that Eq. (37) is singular if inclination is null.

The impact velocity v_{rel} can be computed as:

$$v_{\mathrm{rel}} = \sqrt{v_T^2 + v^2 - 2v_T v\cos\delta} \tag{38}$$

with:

$$\cos\delta = \sin i_T \sin i \cos\Delta\Omega + \cos i_T \cos i \tag{39}$$

where v_T and v are the velocity magnitude of target object and fragments, respectively, i and i_T their inclination, and $\Delta\Omega$ the shift in right ascension of the ascending node between the two orbits. As the fragments orbits are assumed as circular, in order to guarantee intersection

the following condition applies: $v = v_T$. In addition, as the target object orbit is equatorial, Eq. (39) reduces to:

$$\cos\delta = \cos i \tag{40}$$

Therefore, the impact velocity modifies as follows.

$$v_{\text{rel}} = \sqrt{2} v_T \sqrt{1 - \cos i} \tag{41}$$

Combining Eq. (37) and Eq. (41), the impact rate reads as:

$$\dot{\eta} = \sum_j \begin{cases} \frac{A_c N_j v_T}{2\sqrt{2}\pi^2 r_T^2 \, \mathrm{d}r} \frac{1}{\sqrt{1+\cos i_j}} & \text{if } \Omega_j = \lambda_T \\ 0 & \text{otherwise} \end{cases} \tag{42}$$

Fig. 8 depicts the behaviour of the three inclination-dependent functions in Eqs. (37), (41), and (42) between the limits of the effects maps in Fig. 7, i.e., $i \in [0, 90]$ deg. As it can be observed, the impact rate only slightly increases as function of inclination i. Such behaviour is induced by the opposite dependency of the spatial density n_r and the impact velocity v_{rel} on i, when evaluated at the equatorial plane. This, in turn, has the following consequences:

- The effect term, which linearly varies with the impact rate, has a small dependency on inclination for $i > 0$ deg.
- The effect term at $i = 0$ deg is much greater than for any other inclination values. Indeed, for equatorial fragmentations the ejected debris cloud takes short time to randomise over right ascension of the ascending node Ω. As a result, in spite of a smaller impact velocity, induced by the similar orbital plane on which target object and fragments move, the condition on intersection of Eq. (42) is guaranteed for any target object position along its orbit and, thus, the impact probability is considerably higher.

Again, the smaller gradient of the effect term with respect to inclination in the map of catastrophic collisions comes as a consequence of the higher ejection velocity magnitude involved in such events. In fact, the greater impulse guarantees a larger population of fragments to be injected at low inclination values, thus increasing the overall effect value.

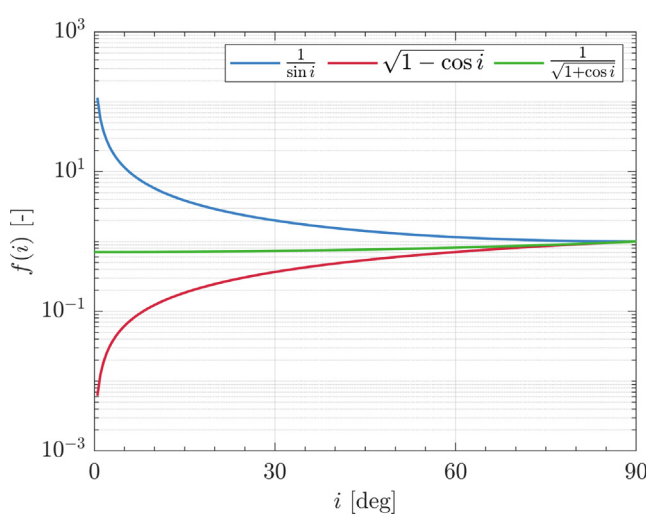

Fig. 8. Dependency of spatial density, impact velocity and impact rate, evaluated at the equatorial plane, on orbit inclination, if intersection is guaranteed.

4.2. High-altitude region

Fig. 9 depicts the effects maps for the high-altitude region of both explosions and catastrophic collisions.

As it can be observed, the parent orbit semi-major axis is the map variable that most affects the risk posed by a fragmentation. In fact, the maximum effect value is caused by the breakups occurring at $a = 26500$ km, where the representative targets with the greatest cumulative cross-sectional area A_c^{tot} are found. By looking at the behaviour of the effect as function of inclination, it can be inferred that the more inclined the fragmentation, the greater the collision risk posed by the associated debris cloud. This behaviour can be justified by the fact that all the representative targets' orbits have a similar and relatively high inclination $i_T \in [55, 70]$ deg. It must be considered that a fragment moving along an orbit with inclination i has a latitude coverage as large as $\phi \in [-i, i]$. As a result, it can potentially collide with a target only when the following condition applies:

$$|\phi_T| \leqslant i \tag{43}$$

with ϕ_T latitude of the target object. This means that the probability of collision caused by a debris cloud whose fragments are characterised by less inclined orbits than the representative targets ones is scaled according to the latitude coverage the cloud guarantees. As for the low-altitude region, there seems to be no clear dependency on the right ascension of the ascending node Ω of the fragmentation orbit. Note that for the high-altitude region this behaviour is further enhanced by the uniform distribution of the representative targets over Ω, as most of the target objects are representative of the navigation constellations.

The computed effects maps are finally adopted for the evaluation of the risk posed by the currently in-orbit active satellites in MEO to the spacecraft population in the same region. To this purpose, the objects' orbital data and mass are retrieved from the DISCOS Database (McLean et al., 2017) and the effect value is computed from the results depicted in Figs. 7 and 9. The effect for the case of catastrophic collisions is scaled based on the spacecraft mass, assuming the mass of the projectile as negligible, according to the second expression in Eq. (26). Instead, as the NASA SBM does not provide a correlation between the scaling factor S and the mass of the object, for the results presented here, S is set according to the following equation:

$$S = \min\left[\left(\frac{M}{M_{\text{ref}}}\right)^{0.75} S_{\text{ref}}, 1\right] \tag{44}$$

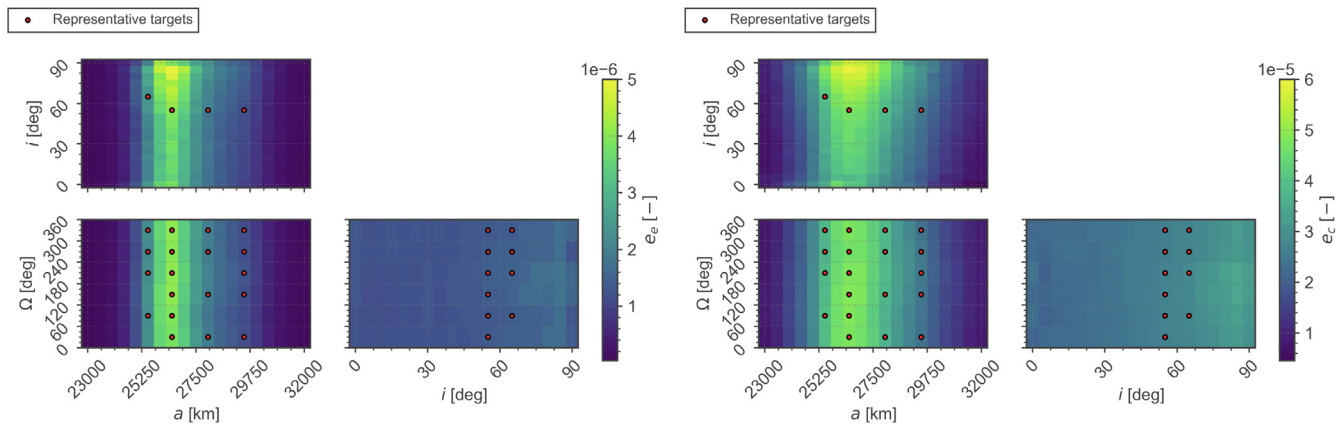

(a) Satellite explosions (b) Catastrophic collisions

Fig. 9. Effects maps in high-altitude MEO against the active objects population in the same region.

Table 4
Active satellites with the largest effect value.

COSPAR ID	Name	a [km]	i [deg]	M [kg]	$e_{\text{exp.}} \times 10^{-3}$	$e_{\text{coll}} \times 10^{-3}$
2019-020A	O3b	14447	0.05	700	0.16366775	1.16893941
2019-056A	GPS	26560	55.59	4400	0.00223060	0.02614939
2012-050B	Beidou	27908	55.31	2300	0.00063209	0.01313449
2009-070C	Cosmos	25507	64.31	1450	0.00059751	0.00924725
2020-075A	Glonass	25506	64.70	974	0.00043584	0.00658295
2015-045A	Galileo	29602	55.76	733	0.00017591	0.00350015
2005-051A	Giove	29731	58.48	600	0.00013977	0.00300396

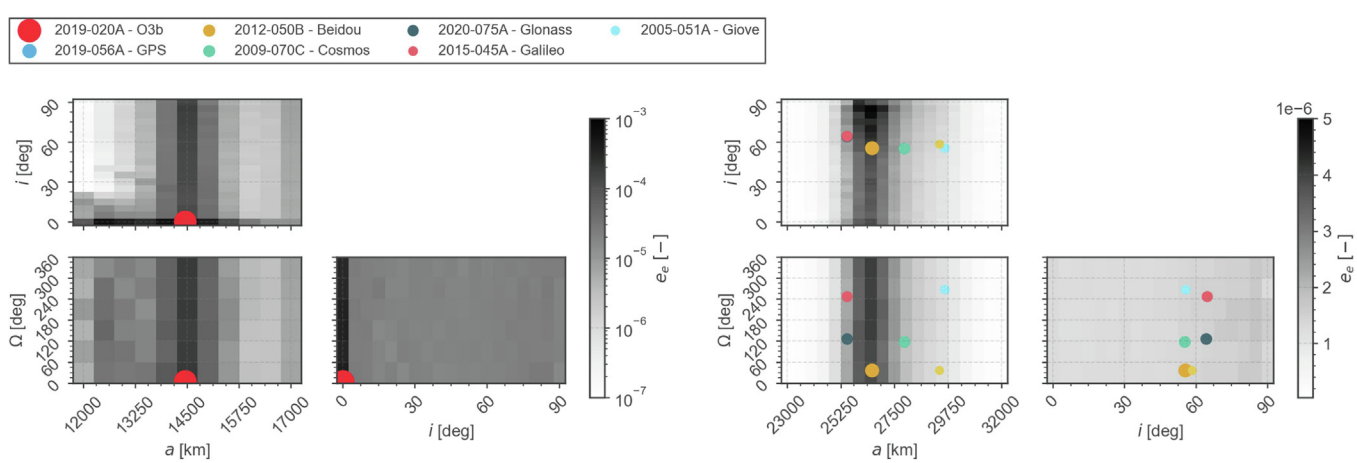

Fig. 10. Effects maps of satellite explosions in MEO against the active objects population in the same region. The markers indicate the active satellites with the largest effect value. The marker size is varied based on the effect.

This implies that the number of fragments, and consequently the effect term, are constrained to vary with mass in the same way for explosions and catastrophic collisions, as long as S is less than unity. The objects with the largest breakup severity values are reported in Table 4 and their location is displayed above the effects maps in Figs. 10 and 11. The size of the markers identifying the objects is varied based on the associated effect value, according to a logarithmic scale. Note that, as all the currently in-orbit active satellites belong to either a constellation or to the same family of spacecraft, only the object with the highest effect value among the satellites of the same constellation/-family is considered. It can be inferred how the severity of the potential breakup of an object of the O3b constellation significantly outnumbers all the navigation satellites in the high-altitude MEO region.

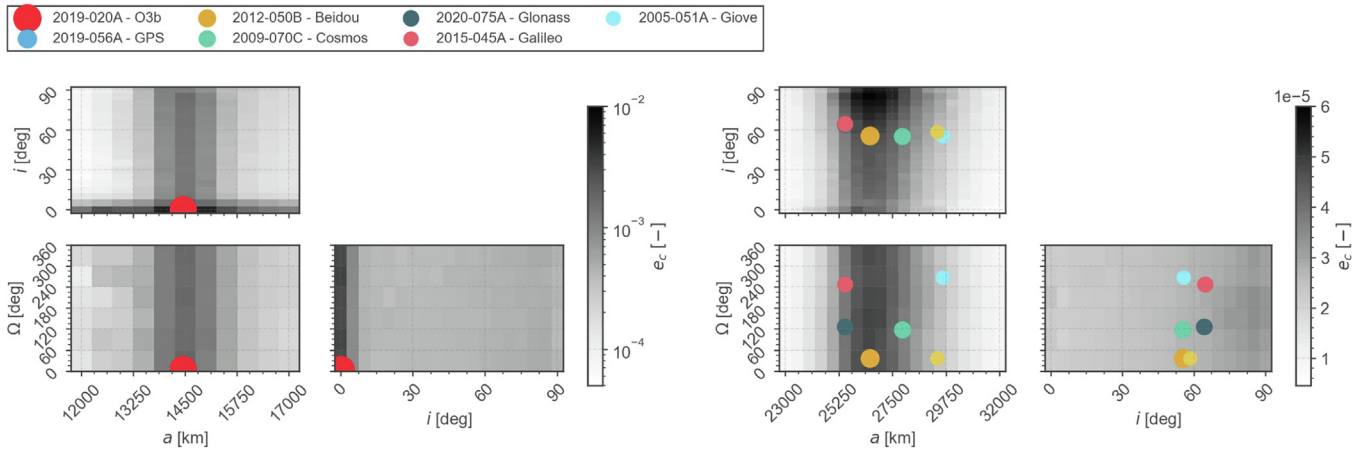

Fig. 11. Effects maps of catastrophic collisions in MEO against the active objects population in the same region. The markers indicate the active satellites with the largest effect value. The marker size is varied based on the effect.

5. Conclusions

Ranking space missions based on how likely they are to contribute to the proliferation of in-orbit fragments is crucial. Among different formulations in the literature, the index ECOB provides quantifiable results, as it evaluates the consequences of an object breakup in terms of collision risk it may pose to spacecraft operations. The same method, which had so far been limited to rate objects in low-Earth orbit, was extended to the medium-Earth orbital region within this work. To achieve this objective, a multi-dimensional model for the propagation of fragments clouds, described as continua, and subsequent evaluation of the collision probability with a set of target objects was implemented. Leveraging the efficiency of a density-based characterisation of fragmentation events, the method allowed the inclusion of centimetre-sized particles in the analyses.

The severity distribution of an object breakup in MEO was computed over the three-dimensional phase space of semi-major axis, inclination and right ascension of the ascending node. The reason for this choice was twofold: first because they are the most representative elements of the missions currently in orbit, and second because of the significant effect that these variables have on the fragments dynamics in this region. Leveraging the fact that the active satellites gather into two well-defined ranges in semi-major axis, the effect term was evaluated for these two regions only, dramatically reducing the computational effort. The impact of satellite explosions and catastrophic collisions for both the low- and high-altitude MEO regions was computed against the satellites population in 2023. The resulting three-dimensional arrays of effect values were depicted in heatmaps representing the increment in collision probability for active objects that a breakup with the specified coordinates would cause. The dependency of the breakup severity on the fragmentation coordinates was extensively studied. Qualitative analyses were performed on the conjunction geometry between fragments and target objects, which served as validation of the complex system at hand. With the population of spacecraft currently orbiting Earth, high-risk regions were found to be confined to well-defined ranges in semimajor axis and inclination, at whose coordinates a fragmentation would result into the highest fragments flux for the most crowded orbital slots. The obtained results were eventually adopted to rank the missions currently in orbit. This analysis demonstrated that the breakup of a satellite of the O3b constellation would have the most detrimental effect, significantly outnumbering any other object in the MEO region.

Declaration of Competing Interest

The authors declare that they have no known competing financial interests or personal relationships that could have appeared to influence the work reported in this paper.

Acknowledgments

This project has received funding from the European Research Council (ERC) under the European Union's Horizon Europe research and innovation programme (grant agreement No 101089265 - GREENSPECIES) and from the European Space Agency contract 4000133981/21/D/KS.

References

Anselmo, L., Pardini, C., 2015. Compliance of the italian satellites in low earth orbit with the end-of-life disposal guidelines for space debris mitigation and ranking of their long-term criticality for the environment. Acta Astronaut., 114, 93–100. URL: https://www.sciencedirect.com/science/article/pii/S0094576515001800. doi: 10.1016/j.actaastro.2015.04.024.

Anselmo, L., Pardini, C., 2016. Ranking upper stages in low earth orbit for active removal. Acta Astronaut., 122, 19–27. URL: https://www.sciencedirect.com/science/article/pii/S0094576516000291. doi: 10.1016/j.actaastro.2016.01.019.

Anselmo, L., Pardini, C., 2017. An index for ranking active debris removal targets in LEO. In: 7th European Conference on Space Debris.

Bastida Virgili, B., Krag, H., 2013. Active debris removal for LEO missions. In: 6th European Conference on Space Debris.

Bombardelli, C., Alessi, E., Rossi, A. et al., 2017. Environmental effect of space debris repositioning. Adv. Space Res., 60(1), 28–37. URL: https://www.sciencedirect.com/science/article/pii/S0273117717302491. doi: 10.1016/j.asr.2017.03.044.

Chobotov, V.A., 1991. Orbital Mechanics, (1st ed.). AIAA Reston. https://doi.org/10.2514/4.862250.

Colombo, C., 2016. Planetary orbital dynamics (PlanODyn) suite for long term propagation in perturbed environment. In: Proc. of the 6th International Conference on Astrodynamics Tools and Techniques.

Colombo, C., 2019. Long-term evolution of highly-elliptical orbits: luni-solar perturbation effects for stability and re-entry. Front. Astron. Space Sci. 6, 34.

Colombo, C., Muciaccia, A., Giudici, L., et al., 2023. Tracking the health of the space debris environment with THEMIS. In: Aerospace Europe Conference 2023-Joint 10th EUCASS-9th CEAS Conference, pp. 1–8.

Colombo, C., Trisolini, M., Gonzalo Gòmez, J., et al., 2021. Assessing the impact of a space mission on the sustainability of the space environment. In: 72nd International Astronautical Congress, pp. 1–10.

Frey, S., Colombo, C., 2021. Transformation of satellite breakup distribution for probabilistic orbital collision hazard analysis. J. Guid., Control, Dynam. 44 (1), 88–105.

Giudici, L., Gonzalo, J.L., Colombo, C., 2024. Density-based in-orbit collision risk model valid for any impact geometry. Acta Astronaut., 219, 785–803. URL: https://www.sciencedirect.com/science/article/pii/S0094576524001930. doi: 10.1016/j.actaastro.2024.03.067.

Giudici, L., Trisolini, M., Colombo, C., 2023. Probabilistic multi-dimensional debris cloud propagation subject to non-linear dynamics. Adv. Space Res., 72(2), 129–151. URL: https://www.sciencedirect.com/science/article/pii/S0273117723003083. doi: 10.1016/j.asr.2023.04.030.

Giudici, L., Trisolini, M., Colombo, C., et al., 2022. Phase space description of the debris' cloud dynamics through a continuum approach. In: 72nd International Astronautical Congress, pp. 1–12.

Gkolias, I., Alessi, E.M., Colombo, C., 2020. Dynamical taxonomy of the coupled solar radiation pressure and oblateness problem and analytical deorbiting configurations. Celest. Mech. Dynam. Astron. 132, 1–18.

Jhon, F., LaSalle, J.P., Sirovich, L., 1981. Partial Differential Equations, 4th ed. Springer, New York.

Johnson, N.L., Krisko, P., Liou, J.-C., et al., 2001. Nasa's new breakup model of evolve 4.0. Adv. Space Res. 28 (9), 1377–1384. https://doi.org/10.1016/S0273-1177(01)00423-9.

Kaufman, B., Dasenbrock, R., 1972. Higher order theory for long-term behavior of earth and lunar orbiters. NRL.

Kaufman, B., Dasenbrock, R., 1973. Semianalytic theory of long-term behavior of earth and lunar orbiters. J. Spacecr. Rock. 10 (6), 377–383.

Kawamoto, S., Nagaoka, N., Kitagawa, Y. et al., 2022. Considerations on the lists of the top 50 debris removal targets. J. Space Saf. Eng., 9(3), 455–463. URL: https://www.sciencedirect.com/science/article/pii/S2468896722000441. doi: 10.1016/j.jsse.2022.05.006.

Letizia, F., Colombo, C., Lewis, H., et al., 2017. Extending the ECOB space debris index with fragmentation risk estimation. In: 7th European Conference on Space Debris.

Letizia, F., Colombo, C., Lewis, H.G., 2016a. Collision probability due to space debris clouds through a continuum approach. J. Guid., Control, Dynam. 39 (10), 2240–2249.

Letizia, F., Colombo, C., Lewis, H.G. et al., 2016b. Assessment of breakup severity on operational satellites. Adv. Space Res., 58(7), 1255–1274. URL: https://www.sciencedirect.com/science/article/pii/S0273117716302393. doi: 10.1016/j.asr.2016.05.036.

Letizia, F., Lemmens, S., 2021. Evaluation of the debris environment impact of the ESA fleet. In: 8th European Conference on Space Debris.

Letizia, F., Lemmens, S., Bastida Virgili, B. et al., 2019. Application of a debris index for global evaluation of mitigation strategies. Acta Astronaut., 161, 348–362. URL: https://www.sciencedirect.com/science/article/pii/S009457651930222X. doi: 10.1016/j.actaastro.2019.05.003.

Lewis, H.G., 2020. Understanding long-term orbital debris population dynamics. J. Space Safety Eng., 7(3), 164–170. URL: https://www.sciencedirect.com/science/article/pii/S2468896720300604. doi: 10.1016/j.jsse.2020.06.006. Space Debris: The State of Art.

McKnight, D., 1990. A phased approach to collision hazard analysis. Adv. Space Res. 10, 385–388. https://doi.org/10.1016/0273-1177(90)90374-9.

McKnight, D., Matney, M., Walbert, K., et al., 2017. Preliminary analysis of two years of the massive collision monitoring activity. In: 68th International Astronautical Congress.

McKnight, D., Witner, R., Letizia, F. et al., 2021. Identifying the 50 statistically-most-concerning derelict objects in LEO. Acta Astronaut., 181, 282–291. URL: https://www.sciencedirect.com/science/article/pii/S0094576521000217. doi: 10.1016/j.actaastro.2021.01.021.

McLean, F., Lemmens, S., Funke, Q. et al., 2017. DISCOS 3: An improved data model for ESA's database and information system characterising objects in space. In: 7th European Conference on Space Debris (pp. 43–52). volume 11.

Muciaccia, A., Giudici, L., Trisolini, M., et al., 2023. Space environment investigation using a space debris index. In: 9th Space Traffic Management Conference.

Omaly, P., Pillet, N., Ruch, V., et al., 2023. CNES space sustainability index. Adv. Space Res., 72(7), 2570–2577. URL: https://www.sciencedirect.com/science/article/pii/S0273117723001023. doi: 10.1016/j.asr.2023.01.062.

Pardini, C., Anselmo, L., 2016. Characterization of abandoned rocket body families for active removal. Acta Astronaut., 126, 243–257. URL: https://www.sciencedirect.com/science/article/pii/S0094576516301333. doi: 10.1016/j.actaastro.2016.04.035.

Pardini, C., Anselmo, L., 2018. Evaluating the environmental criticality of massive objects in LEO for debris mitigation and remediation. Acta Astronaut., 145, 51–75. URL: https://www.sciencedirect.com/science/article/pii/S0094576517317241. doi: 10.1016/j.actaastro.2018.01.028.

Pellegrino, M.M., Scheeres, D.J., Streetman, B.J., 2022. Characterizing doubly-averaged dynamical models in medium earth orbit. Acta Astronaut. 194, 126–144.

Rossi, A., 2008. Resonant dynamics of medium earth orbits: space debris issues. Celest. Mech. Dynam. Astron. 100 (4), 267–286.

Rossi, A., Alessi, E., Valsecchi, G., et al., 2017. A quantitative evaluation of the environmental impact of the mega constellations. In: 7th European Conference on Space Debris.

Rossi, A., Valsecchi, G., Alessi, E., 2015. The criticality of spacecraft index. Adv. Space Res., 56(3), 449–460. URL: https://www.sciencedirect.com/science/article/pii/S0273117715001556. doi: 10.1016/j.asr.2015.02.027. Advances in Asteroid and Space Debris Science and Technology - Part 1.

Ruch, V., Revelin, B., 2020. Space environment index at CNES. In: 8th Satellites end of life and sustainable technologies workshop.

Skoulidou, D.K., Rosengren, A.J., Tsiganis, K., et al., 2019. Medium earth orbit dynamical survey and its use in passive debris removal. Adv. Space Res. 63 (11), 3646–3674.

Vallado, D.A., McClain, W.D., 2007. Fundamentals of astrodynamics and applications, 2nd ed. Springer, Dordrecht.